

Coupled flow and heat transfer of power-law nanofluids on non-isothermal rough rotary disk subjected to magnetic field

Yun-Xian Pei(裴云仙), Xue-Lan Zhang(张雪岚), Lian-Cun Zheng(郑连存)†, and Xin-Zi Wang(王鑫子)
Citation: Chin. Phys. B, 2022, 31 (**6**): 064402. DOI: 10.1088/1674-1056/ac46bd
Journal homepage: http://cpb.iphy.ac.cn; http://iopscience.iop.org/cpb

What follows is a list of articles you may be interested in

Influences of Marangoni convection and variable magnetic field on hybrid nanofluid thin-film flow past a stretching surface

Noor Wali Khan, Arshad Khan, Muhammad Usman, Taza Gul, Abir Mouldi, and Ameni Brahmia
Chin. Phys. B, 2022, 31 (**6**): 064403. DOI: 10.1088/1674-1056/ac3a5d

Construction and mechanism analysis on nanoscale thermal cloak by *in-situ* annealing silicon carbide film

Jian Zhang(张健), Hao-Chun Zhang(张昊春), Zi-Liang Huang(黄子亮), Wen-Bo Sun(孙文博), and Yi-Yi Li(李依依)
Chin. Phys. B, 2022, 31 (**1**): 014402. DOI: 10.1088/1674-1056/ac2809

Thermal apoptosis analysis considering injection behavior optimization and mass diffusion during magnetic hyperthermia

Yun-Dong Tang(汤云东), Jian Zou(邹建), Rodolfo C C Flesch(鲁道夫 C C 弗莱施), Tao Jin(金涛), and Ming-Hua He(何明华)
Chin. Phys. B, 2022, 31 (**1**): 014401. DOI: 10.1088/1674-1056/ac0819

Hierarchical lichee-like Fe_3O_4 assemblies and their high heating efficiency in magnetic hyperthermia

Wen-Yu Li(李文宇), Wen-Tao Li(李文涛), Bang-Quan Li(李榜全), Li-Juan Dong(董丽娟), Tian-Hua Meng(孟田华), Ge Huo(霍格), Gong-Ying Liang(梁工英), and Xue-Gang Lu(卢学刚)
Chin. Phys. B, 2021, 30 (**10**): 104402. DOI: 10.1088/1674-1056/ac0789

First-principles analysis of phonon thermal transport properties of two-dimensional WS_2/WSe_2 heterostructures

Zheng Chang(常征), Kunpeng Yuan(苑昆鹏), Zhehao Sun(孙哲浩), Xiaoliang Zhang(张晓亮), Yufei Gao(高宇飞), Xiaojing Gong(弓晓晶), and Dawei Tang(唐大伟)
Chin. Phys. B, 2021, 30 (**3**): 034401. DOI: 10.1088/1674-1056/abd2a6

Coupled flow and heat transfer of power-law nanofluids on non-isothermal rough rotary disk subjected to magnetic field

Yun-Xian Pei(裴云仙), Xue-Lan Zhang(张雪岚), Lian-Cun Zheng(郑连存)†, and Xin-Zi Wang(王鑫子)

School of Mathematics and Sciences, University of Science and Technology, Beijing 100083, *China*

(Received 1 November 2021; revised manuscript received 26 December 2021; accepted manuscript online 29 December 2021)

We study the coupled flow and heat transfer of power-law nanofluids on a non-isothermal rough rotating disk subjected to a magnetic field. The problem is formulated in terms of specified curvilinear orthogonal coordinate system. An improved BVP4C algorithm is proposed, and numerical solutions are obtained. The influence of volume fraction, types and shapes of nanoparticles, magnetic field and power-law index on the flow, and heat transfer behavior are discussed. The obtained results show that the power-law exponents (PLE), nanoparticle volume fraction (NVF), and magnetic field inclination angle (MFIA) have almost no effects on velocities in the wave surface direction, but have small or significant effects on the azimuth direction. The NVF has remarkable influences on local Nusselt number (LNN) and friction coefficients (FC) in the radial direction and the azimuth direction (AD). The LNN increases with NVF increasing while FC in AD decreases. The types of nanoparticles, magnetic field strength, and inclination have small effects on LNN, but they have remarkable influences on the friction coefficients with positively correlated heat transfer rate, while the inclination is negatively correlated with heat transfer rate. The size of the nanoparticle shape factor is positively correlated with LNN.

Keywords: power-law nanofluids, magnetic field, improved BVP4C algorithm, rough rotating disk

PACS: 47.50.–d, 02.60.Cb, 68.35.Ct, 07.55.Db **DOI:** 10.1088/1674-1056/ac46bd

1. Introduction

The fluid flow and heat transfer on a rotating disk is a common phenomenon in life. It involves many aspects such as rotating heat exchangers,[1] disk drives, atomizers, food processing, and medical services,[2] *etc*. For half a century, many researchers[3–7] have devoted themselves to studying the flow and heat transfer on the rotating disk. Von Kármán[8] discussed the "free disk" problem by assuming it to be axisymmetric and introducing similar transformations. The results show that the circumferential velocity of the fluid increases as the distance from the rotation axis of the disk increases. Cochran and Goldstein[9] conducted the numerical integration to obtain the axial and radial velocity distribution of the fluid in the "free disk" problem based on the similarity transformation proposed by Von Kármán.

Enhancing heat transfer has become an essential demand today, and the active and passive technologies are the two ways to achieve the above goals. The passive technologies such as special geometries, fluid additives, and hot filling are more popular nowadays. The active technologies include magnetic and electric fields.[10] The passive technologies have become important methods in various fields, and relative researches have been carried out as can be found in Refs. [11–13] and others. Wang *et al.*[14] used the main factors of temperature deviation to study the transport of steady-state heat flow. Based on the development of experimental and theoretical researches, it is generally believed that surface discontinuity can improve heat transfer. Periodic discontinuous surfaces can make the thermal boundary layer thinner, thereby improving heat transfer efficiency.[2] Out of this reason, many scholars used periodic surface roughness to study fluid flow and heat transfer. Le Palec[15] and Le Palec *et al.*[16] conducted experimental and theoretical researches by using sinusoidal curve to simulate roughness, and analyzed the heat transfer mechanism of fluids on the rough rotating disk. Yoon *et al.*[17] studied the fluid flow on a sine-shaped rough infinite surface, they found that the torque coefficient and the Nusselt number are positively related to the surface roughness. The thermal boundary condition that the free rotating disk wall exhibits a power-law distribution has been studied by Dorfman and Serazetdinov[18] and Shevchuk.[19] The studies of the uneven temperature distribution on the rough rotating disk can be obtained from Refs. [2,20]. In the two articles the non-uniform temperature distribution of the radius power-law is used. The above researches illustrate the influence of passive technology on heat transfer.

The application of active technologies-magnetic and electric fields to changing the flow and improving the heat transfer has always been a hot research topic. Lu *et al.*[21] studied the effect of anisotropy on the magnetoacoustic response of a magnetoacoustic surface wave resonator. Qu *et al.*[22] carried out a study of the electrical properties of $Ca_3Co_4O_{9+\delta}$ (CCO) materials prepared under a magnetic field. The presence of a magnetic field significantly improved the texture, grain size, and density of the material, thereby increasing the conductivity. Hayat and Nadeem[23] introduced the effect of buoy-

†Corresponding author. E-mail: liancunzheng@ustb.edu.cn

© 2022 Chinese Physical Society and IOP Publishing Ltd

ancy on the flow of incompressible, viscous, and conductive nanofluids at the stagnation point of magnetohydrodynamics on a vertically stretched sheet, by taking into account the effects of induced magnetic fields and viscous dissipation. Li *et al.*[24] studied the propagation of magnetic nanotube domain walls driven by a magnetic field, and the role played by magnetic field in accelerating the motion. Attia and Aboul-Hassan[25] studied the effect of an external uniform magnetic field on the flow caused by a rotating disk, showed that the Hall effect has an influence on the velocity component. Usha *et al.*[26] studied and solved the problem about the loss of thin conductive liquid film on rough surface caused by centrifugation, and found that the existence of magnetic field further enhances the retention of liquid film on rotating disk. The effect of magnetic field on fluid flow on rough rotating wave disk has not been reported in the existing literature.

The traditional heat exchange rate medium has low thermal conductivity, which can no longer meet the increasing requirements for heat exchange in industrial engineering. Nanofluid is a mixture of base fluid and nanoparticles and has good thermal performance,[27] which is often used in drag reduction refrigeration (such as household refrigerators and coolers), boiler exhaust gas recovery, and heat storage, *etc*.[28] Li and Cao[29] combined the Boltzmann transport equation (BTE) equation and solid isotropic material with penalization (SIMP) method to develop a topology optimization method for ballistic diffusion heat conduction. Wang *et al.*[30] revealed the scaling behavior of the thermal conductivity of α-Fe_2O_3 nanowires and analyzed the thermal conductivity of nanomaterials. Xi *et al.*[31] proposed a formula that is generally applicable to the calculation of thermal conductivity of liquids and amorphous solids. Wang *et al.*[32] studied the Leidenfrost effect on the nanoscale, which is helpful in designing the anti-drag surface, self-propelled droplets, and self-assembled nanostructures, and also conducive to other relevant applications. More nano-related researches can be found in Refs. [33–37] and other papers. Mehmood and Iqbal[38] studied the effects of heat absorption and nanoparticles on natural convection heat transfer along the vertical wave cone, showing that the heat transfer rate and friction coefficient are positively related to the volume fraction.

The study of non-Newtonian fluids on rotating disk has always been a hot research topic due to the complexity of its research and the wide range of applications. Alqarni *et al.*[39] used Carreau model to study the instability of non-Newtonian boundary layer flow on a rough rotating disk. Researchers' enthusiasm for studying power-law fluids has not diminished in the studies of many non-Newtonian fluids. Andersson *et al.*[26] modeled the power-law fluid flow caused by a rotating disk. He proposed a reliable numerical calculation method, which can also accurately calculate the shear thickened fluid. Ming *et al.*[40] studied the steady-state flow and thermal effects of fluids on the assumption that the viscosity and thermal conductivity obey power-law characteristics. The most recent researches on the flow of power-law fluids on rotating disks can be found in Refs. [41,42]. Existing studies have shown that little attention has been paid to the power-law fluids on the rough non-isothermal wave disk.

As mentioned above, the Newtonian fluid flow and heat transfer on non-isothermal rough rotating disk have been studied, but the non-Newtonian power-law nanofluid have not been investigated yet. In the present work, we study the power-law Nanofluids on a non-isothermal rough rotary disk subjected to a magnetic field. The problem is formulated, and an improved BVP4C algorithm is proposed to solve nonlinear partial differential equations. The influences of volume fraction, types and shapes of nanoparticles, magnetic field and power-law index on the flow and heat transfer behavior are analyzed.

2. Formulation of problem

The disk (see Fig. 1) with radius b rotates at a fixed angular velocity ω. Rough surface is represented by continuous function $s(\bar{r}) = a_0\cos(2N\pi\bar{r})$; $\bar{r} = r/b$, where a_0 represents the amplitude of the wavy surface, N represents the wave number fitted on the radius b of the disk, and r denotes the radial coordinate.[20] The non-uniform temperature function of the disk surface is expressed as $T_w = T_\infty + C_0 r^{n_*}$, where C_0 is a normal number and n_* is the temperature index, T_w is the disk surface temperature, and T_∞ is the fluid potential flow zone temperature.

We introduce the orthogonal coordinate system (x, θ, y),[2] where x represents the direction of the wave surface of the disk, y denotes the direction perpendicular to the surface, and the azimuth direction is indicated by θ. A magnetic field with an angle of Ω and a magnitude of B is applied to the surface of the disk, where the formula a_0/λ controls the surface morphology of the disk, which is the ratio of amplitude to wavelength. To avoid flow separation and make the control system effective, the boundary layer thickness should be much smaller than the wavelength (*i.e.* $\delta \ll \lambda$) under the same level $a_0/\lambda \leq 0.2$.[16] In this work, 0.4% CMC aqueous solution is chosen and used as the base fluid to study the uniform distribution of nanoparticles (*e.g.*, Al_2O_3, Cu, Ag) in the base fluid. The viscosity coefficient of the nanofluid μ can be obtained from the following formula:

$$\mu = \mu_{nf}\left\{\left(\frac{\partial u_x}{\partial y}\right)^2 + \left(\frac{\partial u_\theta}{\partial y}\right)^2\right\}^{(n-1)/2}, \tag{1}$$

where n is the power-law exponent. Especially when $n = 1$, it is Newtonian fluid, $n < 1$ it is plastic fluid[43] and $n > 1$ it is dilatant fluid.

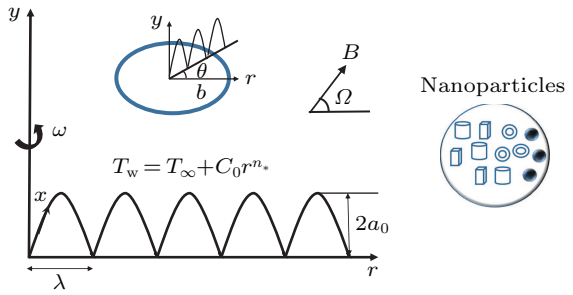


Fig. 1. Schematic diagram of physical model.

Based on the above descriptions, we formulate the governing equations as follows:

Continuity equation:

$$\frac{\partial u_x}{\partial x}+\frac{\partial u_y}{\partial y}+\frac{u_x}{r}\frac{\mathrm{d}r}{\mathrm{d}x}=0; \tag{2}$$

Momentum equation:

$$\begin{aligned} &u_x\frac{\partial u_x}{\partial x}+u_y\frac{\partial u_x}{\partial y}-\frac{u_\theta^2}{r}\frac{\mathrm{d}r}{\mathrm{d}x}\\ &=\left(u_x\frac{\partial u_x}{\partial x}\right)_{y\to\infty}-\frac{\sigma B^2\sin^2\Omega}{\rho_{nf}}(u_x-(u_x)_{y\to\infty})\\ &+\frac{\mu_{nf}}{\rho_{nf}}\left\{\left(\frac{\partial u_x}{\partial y}\right)^2+\left(\frac{\partial u_\theta}{\partial y}\right)^2\right\}^{(n-1)/2}\frac{\partial^2 u_x}{\partial y^2}, \end{aligned} \tag{3}$$

$$\begin{aligned} &u_x\frac{\partial u_\theta}{\partial x}+u_y\frac{\partial u_\theta}{\partial y}+\frac{u_x u_\theta}{r}\frac{\mathrm{d}r}{\mathrm{d}x}\\ &=-\frac{\sigma B^2\sin^2\Omega}{\rho_{nf}}u_\theta\\ &+\frac{\mu_{nf}}{\rho_{nf}}\left\{\left(\frac{\partial u_x}{\partial y}\right)^2+\left(\frac{\partial u_\theta}{\partial y}\right)^2\right\}^{(n-1)/2}\frac{\partial^2 u_\theta}{\partial y^2}; \end{aligned} \tag{4}$$

Energy equation:

$$u_x\frac{\partial T}{\partial x}+u_y\frac{\partial T}{\partial y}=\frac{k_{nf}}{(\rho c_p)_{nf}}\frac{\partial^2 T}{\partial y^2}+\frac{\sigma B^2\sin^2\Omega}{(\rho c_p)_{nf}}u_x^2. \tag{5}$$

The boundary conditions are[20]

$$\begin{aligned} &y=0,\quad u_x=0,\quad u_y=0,\quad u_\theta=\omega r,\quad T_w=T_\infty+C_0 r^{n_*};\\ &y\to\infty,\quad u_x=ar,\quad u_\theta=0,\quad T=T_\infty, \end{aligned} \tag{6}$$

where σ is the magnetic permeability, $u=(u_x,u_y,u_\theta)$ represents the relevant velocity vector.

3. Solution procedure

3.1. Similarity transformation

Owing to the setting of the rough disk surface function, $\mathrm{d}r/\mathrm{d}x$ can be defined as

$$\frac{\mathrm{d}r}{\mathrm{d}x}=\frac{1}{\sqrt{1+4\dfrac{a_0^2\pi^2}{\lambda^2}\sin^2\left(\dfrac{2N\pi r}{b}\right)}}. \tag{7}$$

According to Ref. [20], dimensionless variables and flow functions are defined as follows:

$$\begin{aligned} &f(\varepsilon,\eta)=\frac{\psi(x,y)}{\Lambda r\delta},\quad \Phi(\varepsilon,\eta)=\frac{\phi(x,y)}{\omega r\delta},\\ &\Theta(\varepsilon,\eta)=\frac{T-T_\infty}{T_w-T_\infty}, \end{aligned} \tag{8}$$

with

$$\begin{aligned} &\varepsilon=\frac{x}{\lambda},\quad \eta=\frac{y}{\delta},\quad \Lambda=\sqrt{a^2+w^2},\\ &\delta=\sqrt{\frac{\mu_f\varepsilon}{\rho_f\Lambda R}},\ \text{and}\ R=\frac{r}{\lambda}. \end{aligned} \tag{9}$$

By further simplifying the above, we obtain $\mathrm{d}R/\mathrm{d}\varepsilon=\mathrm{d}r/\mathrm{d}x$. When ε approaches to zero, $\varepsilon/R=\mathrm{d}R/\mathrm{d}\varepsilon=1$.

From Eq. (8) we obtain

$$\psi=\Lambda r\delta f,\quad \phi=\omega r\delta\Phi. \tag{10}$$

The three velocities, namely those velocities along the surface of the disk, the direction of the vertical surface and the direction of the azimuth angle, are obtained from Eqs. (8) and (9), as follows:

$$u_x=\frac{\partial\psi r}{r\partial y}=\frac{\partial\Lambda r^2\delta f}{r\partial y}=\Lambda r f_\eta, \tag{11}$$

$$\begin{aligned} u_y=&-\frac{\partial\psi r}{r\partial x}=-\Lambda\delta\left[\left(\frac{r}{2\lambda\varepsilon}+\frac{3}{2}\frac{\mathrm{d}R}{\mathrm{d}\varepsilon}\right)f+\frac{rf_\varepsilon}{\lambda}\right.\\ &\left.-\frac{r\eta}{\delta}f_\eta\left(\frac{\delta}{2x}-\frac{\delta}{2r}\frac{\mathrm{d}R}{\mathrm{d}\varepsilon}\right)\right], \end{aligned} \tag{12}$$

$$u_\theta=\frac{\partial\phi}{\partial y}=wr\Phi_\eta. \tag{13}$$

Substituting Eqs. (8)–(13) into Eqs. (2)–(6), the dimensionless system of governing equations are as follows:

$$\begin{aligned} &\frac{\mu_{nf}}{\rho_{nf}}\frac{\varepsilon}{R}\frac{1}{\Lambda\delta^2}\left(\frac{\Lambda\lambda R}{\delta}\right)^{n-1}\left[f_{\eta\eta}^2+\left(\frac{\omega}{\Lambda}\Phi_{\eta\eta}\right)^2\right]^{(n-1)/2}f_{\eta\eta\eta}\\ &+\frac{\varepsilon}{R}\frac{\mathrm{d}R}{\mathrm{d}\varepsilon}(\Lambda^2 g_\eta^2-f_\eta^2)+\left(\frac{1}{2}+\frac{3}{2}\frac{\varepsilon}{R}\frac{\mathrm{d}R}{\mathrm{d}\varepsilon}\right)ff_{\eta\eta}\\ &+\left(\frac{a}{\Lambda}\right)^2\frac{\varepsilon}{R}\frac{\mathrm{d}R}{\mathrm{d}\varepsilon}+\frac{\varepsilon}{R}\left(\frac{a}{\Lambda}-f_\eta\right)\frac{\sigma B^2}{\Lambda\rho_{nf}}\sin^2\Omega\\ &=\varepsilon(f_\eta f_{\eta\varepsilon}-f_{\eta\eta}f_\varepsilon), \end{aligned} \tag{14}$$

$$\begin{aligned} &\frac{\mu_{nf}}{\rho_{nf}}\frac{\varepsilon}{R}\frac{1}{\Lambda\delta^2}\left(\frac{\Lambda\lambda R}{\delta}\right)^{n-1}\left[f_{\eta\eta}^2+\left(\frac{\omega}{\Lambda}\Phi_{\eta\eta}\right)^2\right]^{(n-1)/2}\Phi_{\eta\eta\eta}\\ &-2\frac{\varepsilon}{R}\frac{\mathrm{d}R}{\mathrm{d}\varepsilon}f_\eta\Phi_\eta+\left(\frac{1}{2}+\frac{3}{2}\frac{\varepsilon}{R}\frac{\mathrm{d}R}{\mathrm{d}\varepsilon}\right)f\Phi_{\eta\eta}\\ &-\frac{\varepsilon}{R}\frac{\sigma B^2}{\Lambda\rho_{nf}}\sin^2\Omega\,\Phi_\eta=\varepsilon(f_\eta\Phi_{\eta\varepsilon}-\Phi_{\eta\eta}f_\varepsilon), \end{aligned} \tag{15}$$

$$\begin{aligned} &\frac{\Theta_{\eta\eta}}{Pr}+\left(\frac{1}{2}+\frac{3}{2}\frac{\varepsilon}{R}\frac{\mathrm{d}R}{\mathrm{d}\varepsilon}\right)f\Theta_\eta-\frac{\varepsilon}{R}\frac{\mathrm{d}R}{\mathrm{d}\varepsilon}n_* f_\eta\Theta\\ &+\frac{\Lambda r^2\sigma B^2\sin^2\Omega}{(T_w-T_\infty)(\rho c_p)_{nf}}\frac{\varepsilon}{R}f_\eta^2=\varepsilon(f_\eta\Theta_\varepsilon-f_\varepsilon\Theta_\eta). \end{aligned} \tag{16}$$

The corresponding dimensionless boundary conditions are

$$\eta = 0, \quad f = \Phi = f_\eta = \Phi_\eta - 1 = 0, \quad \Theta = 1, \tag{17}$$

$$\eta = \infty, \quad f_\eta = a/\Lambda, \quad \Phi_\eta = 0, \quad \Theta = 0. \tag{18}$$

From Brinkman,[44] we obtain the expression form of nanofluid viscosity μ_{nf},

$$\mu_{nf} = \frac{\mu_{\rm f}}{(1-\varphi)^{2.5}}, \tag{19}$$

where φ is the volume fraction of nanofluid, the dynamic viscosity of the base fluid is $\mu_{\rm f}$. The density of nanofluid ρ_{nf} (Ref. [45]) is related to the volume fraction as follows:

$$\rho_{nf} = \rho_{\rm f}(1-\varphi) + \rho_{\rm s}\varphi, \tag{20}$$

where $\rho_{\rm f}$ and $\rho_{\rm s}$ are the densities of fluid and nano-solid-particles, respectively.

The heat capacity $(\rho c_{\rm p})_{nf}$ of nanofluid is

$$(\rho c_{\rm p})_{nf} = (1-\varphi)(\rho c_{\rm p})_{\rm f} + \varphi(\rho c_{\rm p})_{\rm s}. \tag{21}$$

In addition, according to the Hamilton–Crosser model,[46] the thermal conductivity of the nanofluid is

$$\frac{k_{nf}}{k_{\rm f}} = \zeta\frac{k_{\rm s} + (n_{\rm s}-1)k_{\rm f} - (n_{\rm s}-1)\varphi(k_{\rm f}-k_{\rm s})}{k_{\rm s} + (n_{\rm s}-1)k_{\rm f} + \varphi(k_{\rm f}-k_{\rm s})}, \tag{22}$$

where $k_{\rm f}$ and $k_{\rm s}$ are the thermal conductivities of the base fluid and the nanoparticles, respectively. Equation (22) is applicable to mixtures with almost equal component conductivity. The thermal conductivity ratio of the two-phase mixture is ζ. For the convenience of calculation, it is set to be 1 in this work. The $n_{\rm s}$ is the empirical shape factor of nanoparticles, and can take values of 3, 5.7, 4.9, 3.7 which are corresponding to spherical, platelet, cylindrical, and brick shape, respectively. Various physical parameters of different nanoparticles and base fluid can be seen in Table 1.

Table 1. Different properties of nanoparticles and base fluid (CMC–H_2O).[47,48]

Physical properties	Base fluid	Cu	Al_2O_3	Ag
$c_{\rm p}$ (J/kg·K)	4179	385	765	235
ρ (kg/m^3)	997.1	8933	3970	10500
k (W/mk)	0.613	401	40	429
$\beta\times10^5$ (1/K)	21	1.67	0.85	1.89
σ (s/m)	0.05	59.6×10^6	35×10^6	6.6×10^{-7}

Owing to the radial flow and the azimuthal flow, the shear force along the direction of the curve and the direction of the azimuth angle are written, respectively, as

$$\tau_r = \mu_{nf}\left[\left(\frac{\partial u_x}{\partial y}\right)^2 + \left(\frac{\partial u_\theta}{\partial y}\right)^2\right]^{(n-1)/2}\frac{\partial u_x}{\partial y}\Big|_{y=0}, \tag{23}$$

$$\tau_\theta = \mu_{nf}\left[\left(\frac{\partial u_x}{\partial y}\right)^2 + \left(\frac{\partial u_\theta}{\partial y}\right)^2\right]^{(n-1)/2}\frac{\partial u_\theta}{\partial y}\Big|_{y=0}, \tag{24}$$

where C_{fr} and $C_{f\theta}$ respectively represent the wall friction coefficients in two directions and expressed as

$$C_{fr} = \frac{2\tau_r}{\rho_{nf}r^2\Lambda^2}, \quad C_{f\theta} = \frac{2\tau_\theta}{\rho_{nf}r^2\Lambda^2}. \tag{25}$$

The local Reynolds number Re_r is

$$Re_r = \frac{\Lambda r^2}{\nu} = \Lambda r^2\sqrt{\frac{\rho_{\rm f}\Lambda R}{\mu_{\rm f}x}}. \tag{26}$$

Finally, coefficients of friction in the two directions can be derived as follows:

$$\begin{aligned} Re_r^{1/2}C_{fr} &= 2\frac{\mu_{nf}\rho_{\rm f}}{\rho_{nf}\mu_{\rm f}}\sqrt{\frac{R}{\varepsilon}}\sqrt{\frac{1}{\lambda}}\left(\frac{r}{\delta}\right)^{n-1} \\ &\quad\times\left[(\Lambda f_{\eta\eta})^2 + (\omega\Phi_{\eta\eta})^2\right]^{(n-1)/2} f_{\eta\eta}(\varepsilon,0) \\ &= 2\frac{1}{(1-\varphi)^{2.5}(1-\varphi+\varphi\rho_{\rm s}/\rho_{\rm f})}\sqrt{\frac{R}{\varepsilon}}\sqrt{\frac{1}{\lambda}}\left(\frac{\Lambda r}{\delta}\right)^{n-1} \\ &\quad\times\left[f_{\eta\eta}^2 + \left(\frac{\omega}{\Lambda}\Phi_{\eta\eta}\right)^2\right]^{(n-1)/2} f_{\eta\eta}(\varepsilon,0), \end{aligned} \tag{27}$$

$$\begin{aligned} Re_r^{1/2}C_{f\theta} &= 2\frac{\mu_{nf}\rho_{\rm f}}{\rho_{nf}\mu_{\rm f}}\sqrt{\frac{R}{\varepsilon}}\sqrt{\frac{1}{\lambda}}\left(\frac{r}{\delta}\right)^{n-1}\frac{\omega}{\Lambda} \\ &\quad\times\left[(\Lambda f_{\eta\eta})^2 + (\omega\Phi_{\eta\eta})^2\right]^{(n-1)/2}\Phi_{\eta\eta}(\varepsilon,0) \\ &= 2\frac{1}{(1-\varphi)^{2.5}(1-\varphi+\varphi\rho_{\rm s}/\rho_{\rm f})}\sqrt{\frac{R}{\varepsilon}} \\ &\quad\times\sqrt{\frac{1}{\lambda}}\left(\frac{\Lambda r}{\delta}\right)^{n-1}\frac{\omega}{\Lambda} \\ &\quad\times\left[f_{\eta\eta}^2 + \left(\frac{\omega}{\Lambda}\Phi_{\eta\eta}\right)^2\right]^{(n-1)/2}\Phi_{\eta\eta}(\varepsilon,0). \end{aligned} \tag{28}$$

The expressions of Nusselt number and local Nusselt number are

$$Nu = \frac{q\lambda}{k_{\rm f}(T_{\rm w}-T_\infty)}, \tag{29}$$

$$q = -k_{nf}\left(\frac{\partial T}{\partial y}\right)\Big|_{y=0}, \tag{30}$$

$$Re_\Lambda = \frac{\Lambda\lambda^2}{\nu}, \tag{31}$$

$$Re_\Lambda^{-1/2}Nu = -\frac{k_{nf}}{k_{\rm f}}\sqrt{\frac{R}{\varepsilon}}\Theta_\eta(\varepsilon,0), \tag{32}$$

where q is the wall heat flux, Re_Λ represents the rotational Reynolds number, and ν is the dynamic viscosity coefficient of fluid.

Le Palec[15] has shown that taking the area of the flat disk as a reference, we can increase Nusselt number of the wave disk by increasing the area ratio $S/\pi b^2$ (S refers to the wavy

disk area), thereby increasing the heat transfer. The expressions of Nusselt numbers (average and modified) can be derived as follows:

$$\overline{Nu}Re_{\Lambda}^{-1/2} = \frac{1}{S}\int_S Re_{\Lambda}^{-1/2}Nu\mathrm{d}S, \tag{33}$$

$$\overline{Nu_{\mathrm{p}}} = \overline{Nu}\frac{S}{\pi b^2}, \tag{34}$$

$$\begin{aligned}\overline{Nu_{\mathrm{p}}}Re_{\Lambda}^{-1/2} &= \frac{1}{S}\int_S Re_{\Lambda}^{-1/2}Nu\mathrm{d}S\frac{S}{\pi b^2}\\ &= \frac{1}{\pi b^2}\int_S Re_{\Lambda}^{-1/2}Nu\mathrm{d}S.\end{aligned} \tag{35}$$

3.2. Method solving

In Ref. [2], Mehmood *et al*. used the Keller–Box method to solve two-dimensional nonlinear partial differential equations. The Keller–Box method needs to difference between two independent variables, and uses the chasing method to solve the matrix equation according to the Newton iteration method, which is labor-intensive and time-consuming.

The existing BVP4C algorithm can be used only to solve one-dimensional differential equations. However, in this work, we formulate the two-dimensional nonlinear partial differential equations. In order to solve these equations here, we introduce the idea of difference to transform the two-dimensional variable into the equations with derivatives with respect to only one variable, so that the existing BVP4C algorithm can be used to solve the equations. This improved method gets rid of the limitations of BVP4C. In this work, the improved BVP4C algorithm is used to solve the formulated equations and the obtained solutions are compared with the numerical solutions in the literature, thereby verifying their good consistence and the effectiveness of the method (see Table 2).

Table 2. Comparison between numerical simulation results from two algorithms.

		$n_*=-2$		$n_*=0$	
a/ω	Pr	Muhammad[2]	Improved BVP4C algorithm	Muhammad[2]	Improved BVP4C algorithm
0	0.1	0.0	0.0	0.0766	0.07662
	1	0.0	0.0	0.3963	0.39630
	10	0.0	0.0	1.1341	1.13411
	100	0.0	0.0	2.6871	2.68712
0.5	0.71	0.0	0.0	0.4194	0.41940
	1	0.0	0.0	0.4815	0.48151
1	0.71	0.0	0.0	0.4897	0.48971
	1	0.0	0.0	0.5536	0.55362
10	0.71	0.0	0.0	0.6381	0.63813
	1	0.0	0.0	0.7270	0.72700

3.3. Algorithm solution steps

According to the improved BVP4C algorithm idea, we need to difference one of the two-dimensional variables. For the variables ε and η in the two directions, we choose the difference operation on the derivative in the ε direction. Let d be the step size in the direction, the derivatives of functions $f(\varepsilon,\eta)$, $\Phi(\varepsilon,\eta)$, and $\Theta(\varepsilon,\eta)$ in the ε direction are subjected to difference operation, where n is the position of the node during the difference operation. Simplifying Eqs. (14)–(16) by difference yields the following equations:

$$\begin{aligned}&\frac{\mu_{nf}}{\rho_{nf}}\frac{\varepsilon}{R}\frac{1}{\Lambda\delta^2}\left(\frac{\Lambda r}{\delta}\right)^{n-1}\left[f_{\eta\eta}^2+\left(\frac{\omega}{\Lambda}\Phi_{\eta\eta}\right)^2\right]^{(n-1)/2}f_{\eta\eta\eta}\\ &+\frac{\varepsilon}{R}\frac{\mathrm{d}R}{\mathrm{d}\varepsilon}\left(\Lambda^2 g_\eta^2-f_\eta^2\right)+\left(\frac{1}{2}+\frac{3}{2}\frac{\varepsilon}{R}\frac{\mathrm{d}R}{\mathrm{d}\varepsilon}\right)ff_{\eta\eta}\\ &+\left(\frac{a}{\Lambda}\right)^2\frac{\varepsilon}{R}\frac{\mathrm{d}R}{\mathrm{d}\varepsilon}+\frac{\varepsilon}{R}\left(\frac{a}{\Lambda}-f_\eta\right)\frac{\sigma B^2}{\Lambda\rho_{nf}}\sin^2\Omega\\ &=\varepsilon\left(f_\eta\frac{f_\eta^n-f_\eta^{n-1}}{d}-f_{\eta\eta}\frac{f^n-f^{n-1}}{d}\right),\end{aligned} \tag{36}$$

$$\begin{aligned}&\frac{\mu_{nf}}{\rho_{nf}}\frac{\varepsilon}{R}\frac{1}{\Lambda\delta^2}\left(\frac{\Lambda r}{\delta}\right)^{n-1}\left[f_{\eta\eta}^2+\left(\frac{\omega}{\Lambda}\Phi_{\eta\eta}\right)^2\right]^{(n-1)/2}\Phi_{\eta\eta\eta}\\ &-2\frac{\varepsilon}{R}\frac{\mathrm{d}R}{\mathrm{d}\varepsilon}f_\eta\Phi_\eta+\left(\frac{1}{2}+\frac{3}{2}\frac{\varepsilon}{R}\frac{\mathrm{d}R}{\mathrm{d}\varepsilon}\right)f\Phi_{\eta\eta}\\ &-\frac{\varepsilon}{R}\frac{\sigma B^2}{\Lambda\rho_{nf}}\sin^2\Omega\Phi_\eta\\ &=\varepsilon\left(f_\eta\frac{\Phi_\eta^n-\Phi_\eta^{n-1}}{d}-\Phi_{\eta\eta}\frac{f^n-f^{n-1}}{d}\right),\\ &\frac{\Theta_{\eta\eta}}{Pr}+\left(\frac{1}{2}+\frac{3}{2}\frac{\varepsilon}{R}\frac{\mathrm{d}R}{\mathrm{d}\varepsilon}\right)f\Theta_\eta-\frac{\varepsilon}{R}\frac{\mathrm{d}R}{\mathrm{d}\varepsilon}n_*f_\eta\Theta\\ &+\frac{\Lambda r^2\sigma B^2\sin^2\Omega}{(T_{\mathrm{w}}-T_\infty)(\rho c_{\mathrm{p}})_{nf}}\frac{\varepsilon}{R}f_\eta^2\\ &f(\varepsilon,\eta),\Phi(\varepsilon,\eta),\Theta(\varepsilon,\eta)\\ &=\varepsilon\left(f_\eta\frac{\Theta^n-\Theta^{n-1}}{d}-\frac{f^n-f^{n-1}}{d}\Theta_\eta\right).\end{aligned} \tag{37, 38}$$

4. Results and discussion

Now, we solve Eqs. (14)–(16) with boundary conditions Eqs. (17) and (18) by our improved BVP4C algorithm. The

numerical results are shown and analyzed in the following.

Figures 2(a)–2(d) show for each fixed power-law index n ($n = 0.5$, 1, and 1.2, shear thinning, Newtonian fluid and shear thickening), the effects of nanoparticle volume fractions (0%, 1%, 2%, 4%) on velocity field. It is found that for each fixed n and different values of nanoparticle volume fraction (NVF) Φ, the velocity profiles are almost overlapped, which means that the volume fraction has almost no effect on velocity field. However, we see that the azimuthal velocity changes remarkably with the value of n, which can also be seen from Fig. 3. By taking the peak velocity value in the azimuth direction when the volume fraction is 4% in Figs. 2(b)–2(d), it can be seen that the difference is very small, indicating that the volume fraction has almost no effect on the velocity in this direction. Figures 2(c) and 2(d) show that under the influence of nanometer volume fraction and power-law exponent, the power-law exponent has a greater influence on axial velocity. In the three representative different nanofluid types, the images have more obvious differences. The larger the volume fraction, the smaller the azimuthal friction coefficient between fluid molecules is (see Fig. 5), which promotes fluid flow but the effect is insignificant.

Figures 3(a) and 3(b) illustrate the effects of power-law exponents (PLEs) ($n = 0.3$, 0.5, 1, 1.2, and 1.5) on velocity field. The results show the PLE has almost no effect on the velocity in the x direction (Fig. 3(a)). However, it has very remarkable effect on the velocity profile in θ direction (Fig. 3(b)). The increase of the power-law exponent will lead the axial shear force to increase, which in turn affects the axial velocity of the fluid. The thickness of the fluid dynamic boundary layer becomes thinner with the increase of PLE, and the azimuth velocity is greatly affected by the thickness. The change in flow rate occurs significantly in the axial direction to supplement the radial outflow.

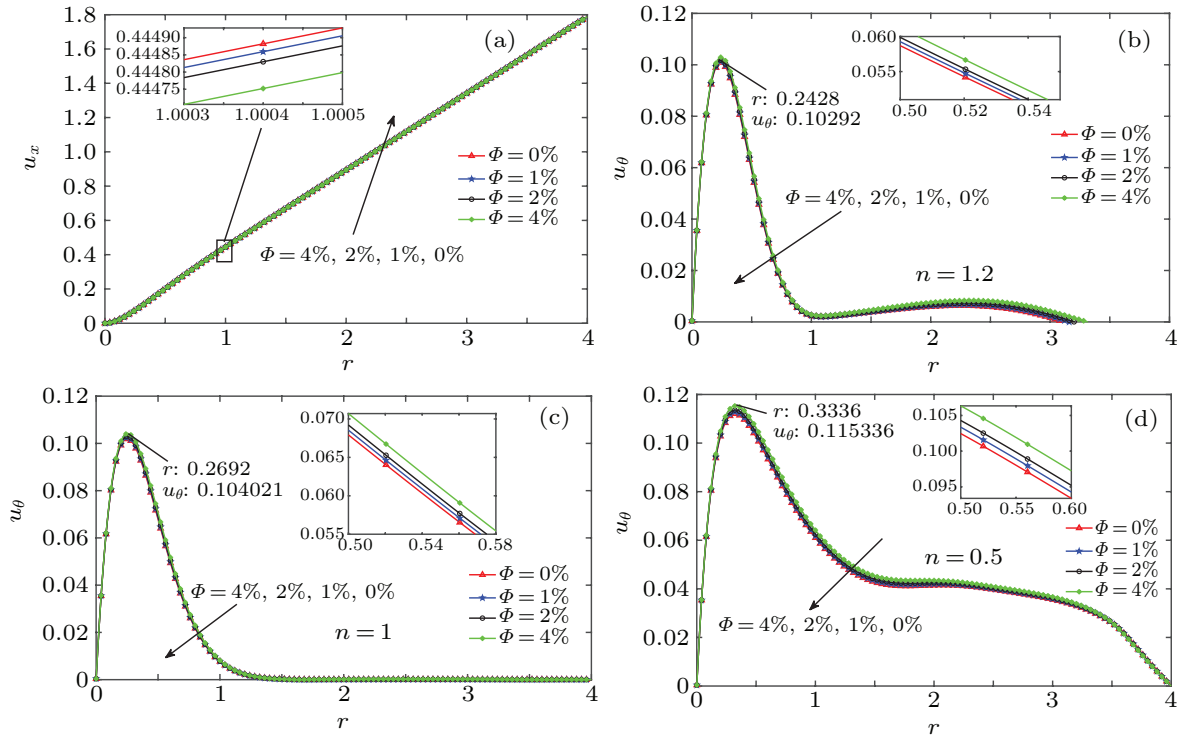


Fig. 2. Effects of different volume fractions on velocities for Al_2O_3/CMC nanofluid.

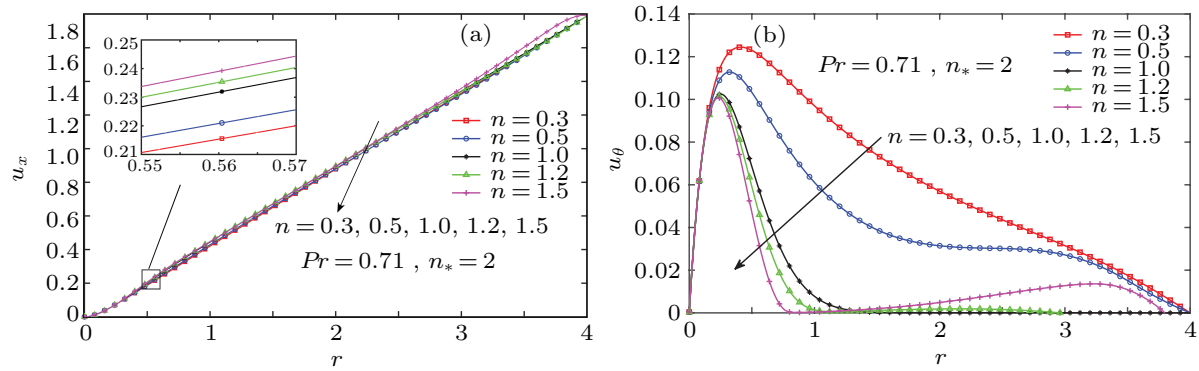


Fig. 3. Effects of different PLEs on velocities for Al_2O_3/CMC nanofluid.

Figures 4(a)–4(d) reveal the effects of magnetic field inclination angle on the velocity profile both in the x direction and in the θ direction for fixed power-law index n. It can be seen that the angle Ω has almost no effect on u_x, but has very strong influence on u_θ. For each fixed value of n, the velocity profile u_θ decreases as the inclination angle Ω increases. From Figs. 4(b)–4(d) for the four different inclination angles, the peak value of u_θ is present when $\Omega = \pi/6$ and the velocity profile of plastic fluid is higher than the other three ones. The greater the inclination angle of the magnetic field, the stronger the effect of the Lorentz force on the surface of the fluid is, which slows down the flow of the fluid. For the azimuth direction velocity, the wall shear stress decreases with the magnetic field angle increasing.

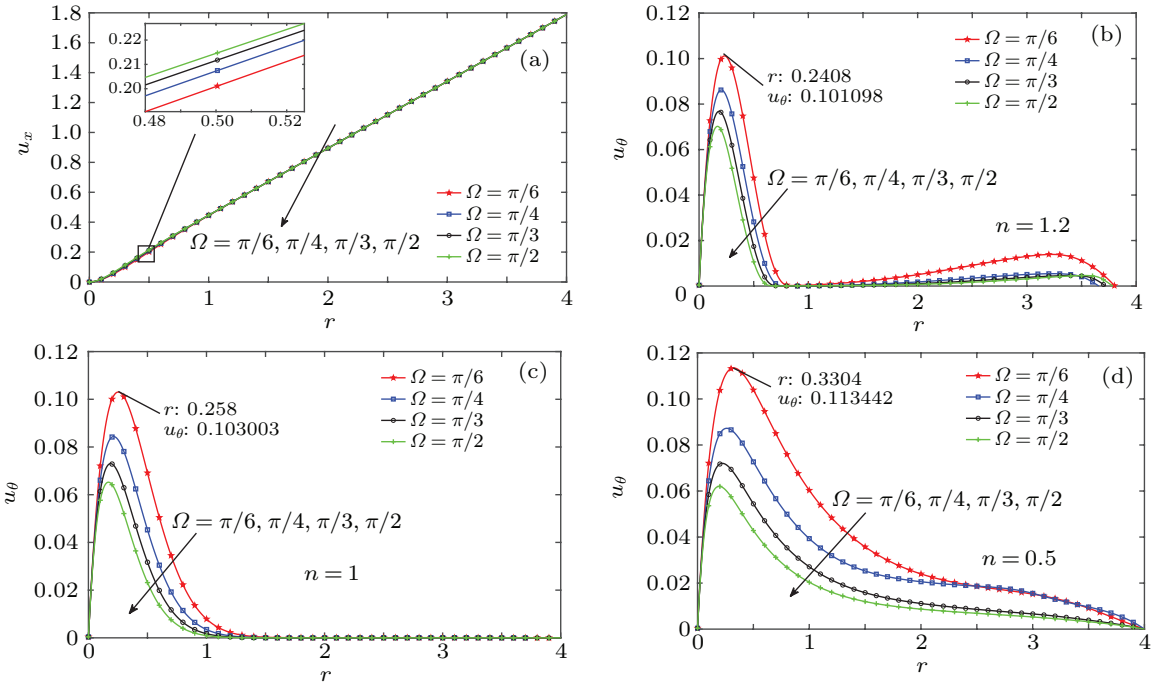


Fig. 4. Effects of different magnetic field inclinations on velocity for Al_2O_3/CMC nanofluid.

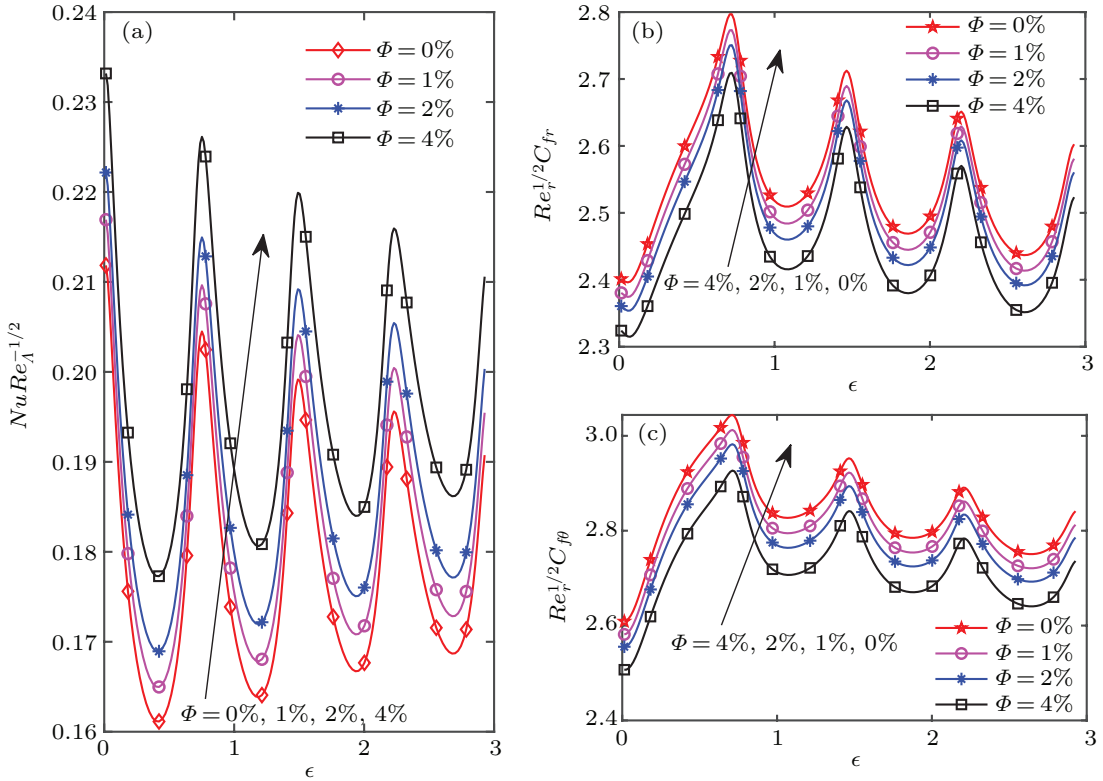


Fig. 5. Variations of local Nusselt number and friction coefficients with nanoparticle volume fraction value (Al_2O_3/CMC nanofluid, $Pr = 0.71$, $n_* = 2$, $n = 2$).

Figures 5(a)–5(c) display the effects of nanoparticle volume fraction Φ on local Nusselt number $NuRe_{\Lambda}^{-1/2}$ and friction coefficients: $Re_r^{1/2}C_{\mathrm{fr}}$ and $Re_r^{1/2}C_{\mathrm{f}\theta}$, in r direction and θ direction. It is found that the volume fractions Φ has a very strong influence on the parameters of these physical properties. These parameters fluctuate due to the special topography of the surface. The $NuRe_{\Lambda}^{-1/2}$ increases with Φ increasing, but the friction coefficient in the r direction and the θ direction: $Re_r^{1/2}C_{\mathrm{fr}}$ and $Re_r^{1/2}C_{\mathrm{f}\theta}$, decrease with Φ increasing. The value of $Re_r^{1/2}C_{\mathrm{f}\theta}$ is slightly larger than that of $Re_r^{1/2}C_{\mathrm{fr}}$. The value of Φ affects the thermal conductivity ratio, and thus the local Nusselt number is obtained from Eq. (32). From Table 3 it can follow that when the type and shape of nanoparticles are fixed, the thermal conductivity ratio increases with the particle volume fraction increasing. The characteristics of improving heat transfer after adding nanoparticles are better explained.

Figures 6(a)–6(c) show the effects of different nanoparticle types on local Nusselt number $NuRe_{\Lambda}^{-1/2}$ and friction coefficients in the r direction and the θ direction: $Re_r^{1/2}C_{\mathrm{fr}}$ and $Re_r^{1/2}C_{\mathrm{f}\theta}$. It can see that the type of particles has almost no effect on $NuRe_{\Lambda}^{-1/2}$, but it has strong effects on both $Re_r^{1/2}C_{\mathrm{fr}}$ and $Re_r^{1/2}C_{\mathrm{f}\theta}$. For the friction coefficients, Al_2O_3 particles have the biggest magnitude and Ag particles have the smallest magnitude, showing that the type of nanoparticles has almost no effect on the heat transfer efficiency, but it has remarkable effect on the friction coefficient. For the fixed nanoparticles shape factor and volume fraction, it can be seen from Eq. (22) and Table 1 that the types of nanoparticles corresponding to the thermal conductivity ratio from small value to large value are in the order of Al_2O_3, Cu, Ag.

Table 3. Values of under different volume fractions and shape factors.

Type	Shape	n_{s}	Graphic	Nanoparticle volume fraction				
				0%	1%	2%	3%	4%
Al_2O_3	spherical	3		1	1.028938	1.058440	1.088523	1.119202
	bricks	3.7		1	1.035319	1.071319	1.108029	1.145442
	cylinder	4.9		1	1.045955	1.092784	1.140523	1.189142
	platelet	5.7		1	1.052841	1.106678	1.161517	1.217413
Cu	spherical	3		1	1.012033	1.024309	1.036838	1.049627
	bricks	3.7		1	1.037161	1.075076	1.113769	1.153262
	cylinder	4.9		1	1.049123	1.099240	1.150383	1.202584
	platelet	5.7		1	1.057073	1.115312	1.174717	1.235369
Ag	spherical	3		1	1.030172	1.060957	1.092375	1.124444
	bricks	3.7		1	1.037175	1.075104	1.113812	1.153321
	cylinder	4.9		1	1.049147	1.099291	1.150459	1.202686
	platelet	5.7		1	1.057105	1.115366	1.174819	1.235499

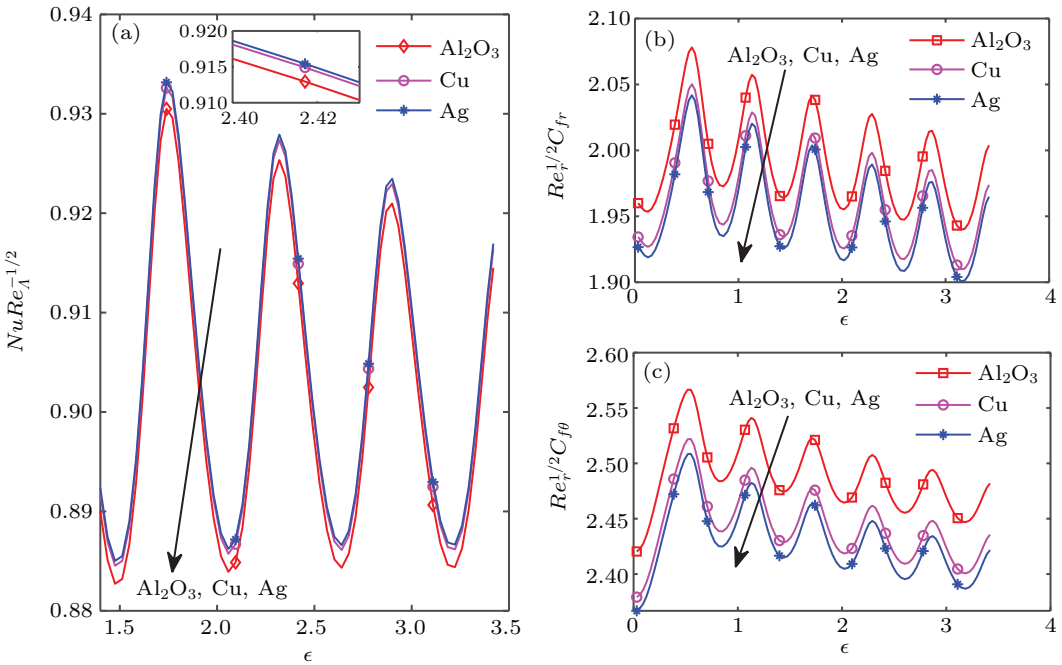


Fig. 6. Variations of local Nusselt number and friction coefficients with type of nanoparticles ($Pr = 0.71$, $n_* = 2$, $n = 2$).

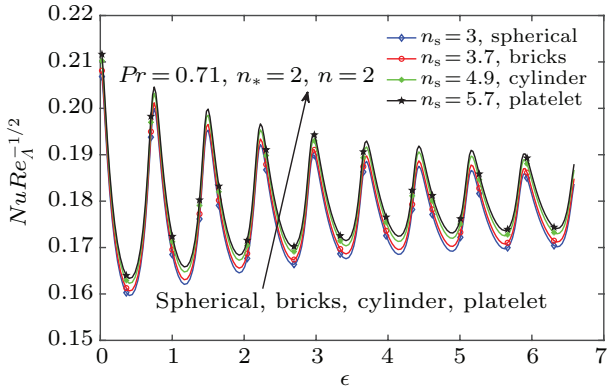


Fig. 7. Variations of local Nusselt number with nanoparticle type for Al_2O_3/CMC nanofluid ($Pr = 0.71$, $n_* = 2$, $n = 2$).

Figure 7 displays the effects of shapes of nanoparticles (platelet, cylinder, brick and spherical) on local Nusselt number $NuRe_\Lambda^{-1/2}$. It is seen that the shape of nanoparticles used here has a slight effect on local Nusselt number, where the curves in the image are for the shapes of platelet, cylinder, brick and spherical from top to bottom. From Eq. (22), we know that the shape factor n_s affects the thermal conductivity. Through calculation, we obtain different values of k_{nf}/k_f as shown in Table 3. In the case of fixed nanoparticle type and volume fraction, the four shape factors corresponding to the thermal conductivity from small to large value are spherical, brick, cylindrical, platelet shape. The larger the shape factor value, the larger the corresponding thermal conductivity ratio is, so the greater the local heat transfer efficiency. The platelet-shape nanoparticles have the largest thermal conductivity ratio, large local Nusselt number, and high local heat transfer efficiency.

Figures 8 and 9 show effects of magnetic field strength B and inclination Ω on physical property parameters $NuRe_\Lambda^{-1/2}$, $Re_r^{1/2}C_{fr}$, and $Re_r^{1/2}C_{f\theta}$. We can see from the figures that B and Ω have small effects on the local Nusselt number $NuRe_\Lambda^{-1/2}$ but have very significant influences on friction coefficients $Re_r^{1/2}C_{fr}$ and $Re_r^{1/2}C_{f\theta}$. Both friction coefficients in the two directions are positively correlated with B and Ω. The magnetic field strength increases convective heat transfer, and the magnetic inclination angle affects the friction coefficients and thus the velocity. It can be seen from Eq. (32) that the change of magnetic field strength mainly affects the temperature and thus the efficiency of convective heat transfer.

Figure 10 reveals variations of average Nusselt numbers $\overline{Nu}Re_\Lambda^{-1/2}$ and $\overline{Nu}_pRe_\Lambda^{-1/2}$ with different values of parameters such as volume fraction Φ, magnetic field strength B, and magnetic field inclination Ω. Figures 10(a)–10(c) respectively show that the average Nusselt numbers increases as Φ increases, increase as B increases, but decrease as Ω increases. The value of $\overline{Nu}_pRe_\Lambda^{-1/2}$ is bigger than $\overline{Nu}Re_\Lambda^{-1/2}$, which can also can be proven from Eqs. (33)–(35). The above facts show that Φ and B can increase the average heat transfer rate, but Ω is negatively related to the heat transfer rate. $\overline{Nu}_pRe_\Lambda^{-1/2}$ increases with the increase of the roughness of the disk, which shows that the degree of convective heat transfer increases with the increase of the roughness of the disk.

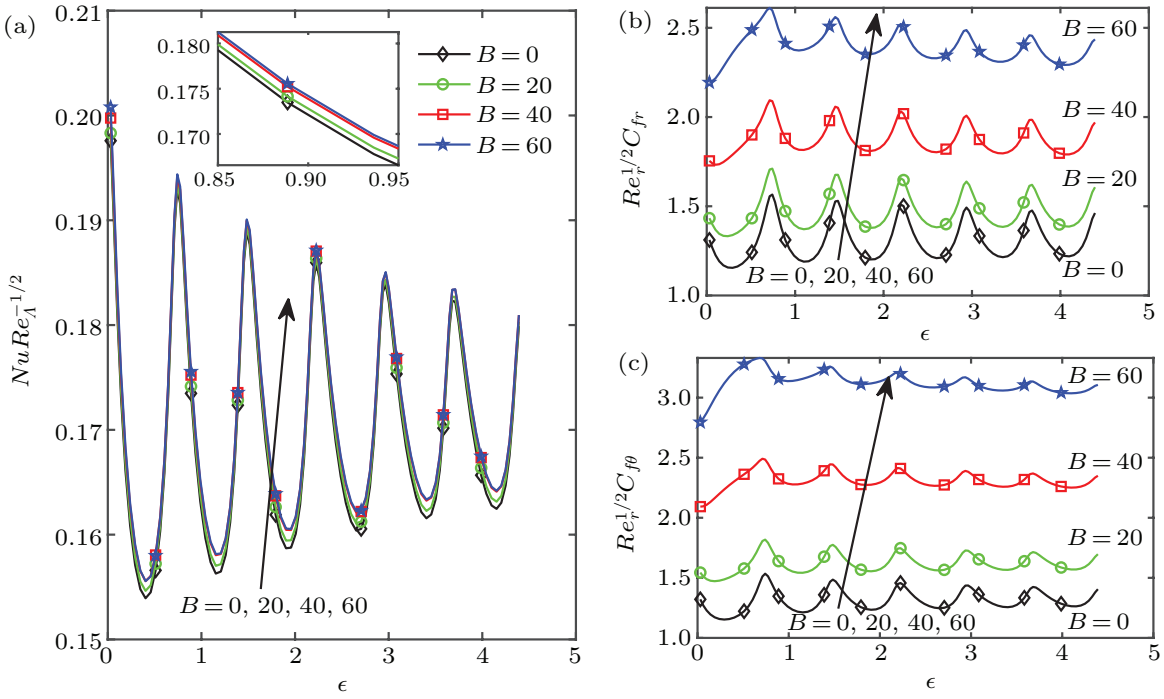


Fig. 8. Variations of local Nusselt number and friction coefficients under different values of magnetic field strength (Al_2O_3/CMC nanofluid, $Pr = 0.71$, $n_* = 2$, $n = 2$).

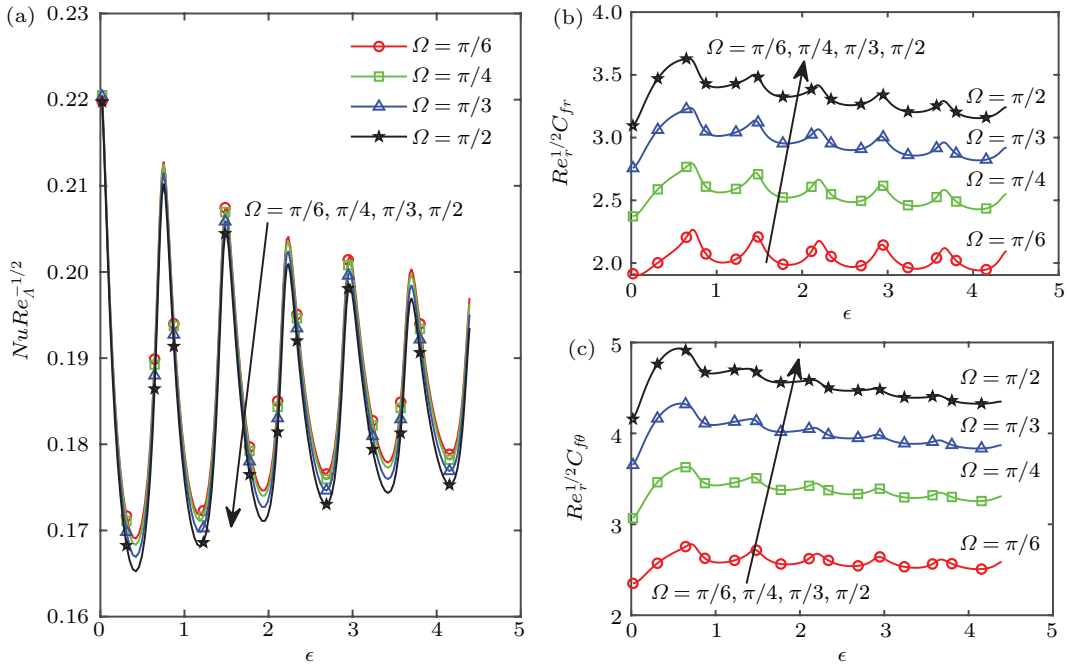


Fig. 9. Variations of local Nusselt number and friction coefficients under different value of magnetic field angle (Al_2O_3/CMC nanofluid, $Pr=0.71$, $n_*=2$, $n=2$).

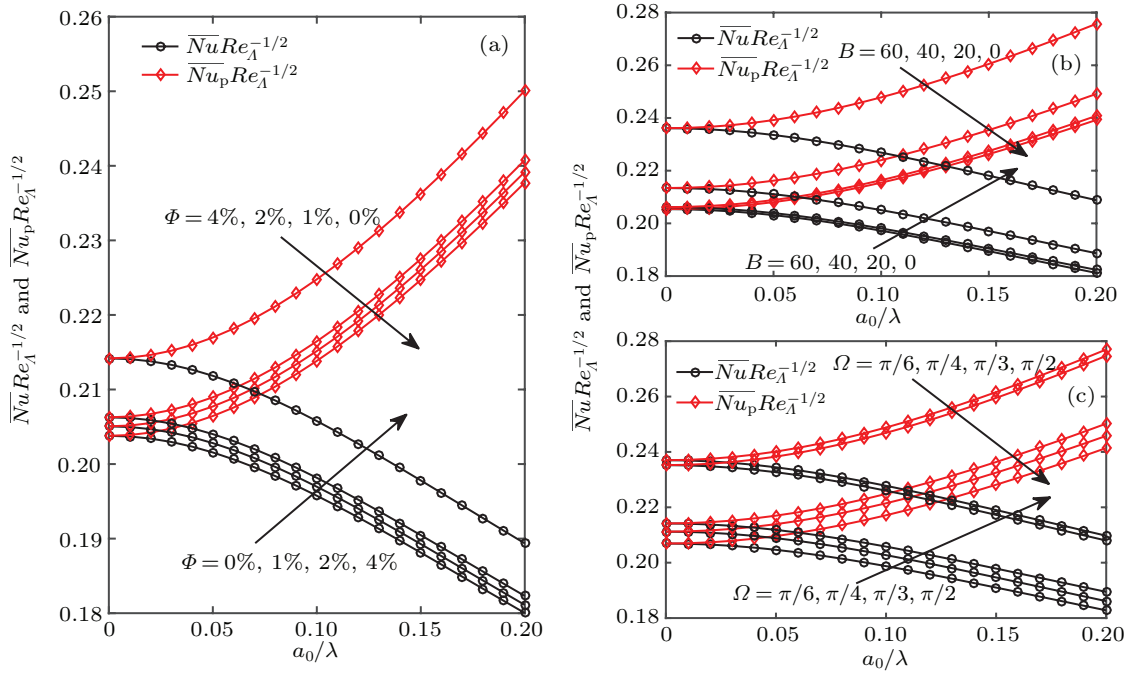


Fig. 10. Variations of average Nusselt numbers ($\overline{Nu}Re_{\Lambda}^{-1/2}$ and $\overline{Nu}_pRe_{\Lambda}^{-1/2}$) under different parameters (Al_2O_3/CMC nanofluid, $Pr=0.71$, $n_*=2$, $n=2$).

5. Conclusions

In this paper, we have studied the coupled flow and heat transfer of power-law Nanofluids on a non-isothermal rough rotating disk subjected to magnetic field. The problems are formulated in nonlinear partial differential equations and solved by the proposed improved BVP4C algorithm. The fluid flow and heat transfer characteristics are analyzed and discussed by numerical results. The main conclusions are presented as follows.

(i) The nanoparticle volume fraction Φ has almost no effect on the velocity field. Different PLE and MFIA have almost no effect on the velocity in the x direction, but both have greater influences on the velocity in the θ direction. The u_θ decreases with the augment of the PLE n and the MFIA Ω.

(ii) Owing to the special morphology (sinusoidal) of the disk surface, the local Nusselt number $NuRe_{\Lambda}^{-1/2}$ and local friction coefficients ($Re_r^{1/2}C_{\rm fr}$ and $Re_r^{1/2}C_{\rm f\theta}$) show the fluctuating trends under different parameters such as nanoparticle volume fraction Φ, magnetic field angle Ω, magnetic field strength B, and nanoparticle type and shape. The volume frac-

tion has a strong influence on the three physical parameters. $NuRe_{\Lambda}^{-1/2}$ increases as Φ increases, $Re_r^{1/2}C_{\mathrm{fr}}$ and $Re_r^{1/2}C_{\mathrm{f}\theta}$ are negatively correlated with Φ.

(iii) The type of nanoparticles has almost no effect on $NuRe_{\Lambda}^{-1/2}$, but has greater influences on $Re_r^{1/2}C_{\mathrm{fr}}$ and $Re_r^{1/2}C_{\mathrm{f}\theta}$. For the friction coefficients, Al_2O_3 particles have the largest magnitude, while Ag particles have the smallest friction coefficient. The shape of nanoparticles affects $NuRe_{\Lambda}^{-1/2}$. Platelet-shaped particles have the largest curve value, and spherical particles have the smallest curve value.

(iv) Magnetic field angle Ω and magnetic field strength B have little effect on $NuRe_{\Lambda}^{-1/2}$, but have greater influences on $Re_r^{1/2}C_{\mathrm{fr}}$ and $Re_r^{1/2}C_{\mathrm{f}\theta}$. The two parameters are positively related to the coefficient of friction.

(v) The average Nusselt number $\overline{Nu}Re_{\Lambda}^{-1/2}$and the modified average Nusselt number $\overline{Nu_{\mathrm{p}}}Re_{\Lambda}^{-1/2}$ are positively correlated with Φ and B, but negatively correlated with Ω. The magnetic field strength and volume fraction can increase the heat transfer rate of the wave disk.

Acknowledgement

Project supported by the National Natural Science Foundations of China (Grant No. 11772046).

References

[1] Mochizuki S and Yang W J 1981 *J. Heat Transfer* **103** 212
[2] Mehmood A, Usman M and Weigand B 2019 *Int. J. Heat Mass Transfer* **129** 96
[3] Bödewadt U T 1940 *J. Appl. Math. Mech.* **20** 241
[4] Batchelor G K 1951 *Q. J. Mech. Appl. Math.* **4** 29
[5] Stewartson K 1953 *Math. Proc. Cambridge Philos. Soc.* **49** 333
[6] Alzahrani F and Ijaz Khan M 2021 *Alexandria Eng. J.* **61** 3679
[7] Raju S S K, Babu M J and Raju C S K 2021 *Chin. J. Phys.* **72** 499
[8] Kármán Th V 1921 *J. Appl. Math. Mech.* **1** 233
[9] Cochran W G and Goldstein S 1934 *Math. Proc. Cambridge Philos. Soc.* **30** 365
[10] Hayat T, Muhammad T, Shehzad S A and Alsaedi A 2017 *Comput. Methods Appl. Mech. Eng.* **315** 467
[11] Zhang L M, Jiao B B, Yun S C, Kong Y M, Ku C W and Chen D P 2017 *Chin. Phys. Lett.* **34** 025101
[12] Jin Q X, Liu B, Liu Y, Wang W W, Wang H, Xu Z, Gao D, Wang Q, Xia Y Y, Song Z T and Feng S L 2016 *Chin. Phys. Lett.* **33** 098502
[13] Hu R, Hu J Y, Wu R K, Xie B, Yu X J and Luo X B 2016 *Chin. Phys. Lett.* **33** 044401
[14] Wang C, Wang L Q and Ren J 2021 *Chin. Phys. Lett.* **38** 010501
[15] Georges Le P 1989 *Int. Commun. Heat Mass Transfer* **16** 107
[16] Le Palec G, Nardin P and Rondot D 1990 *Int. J. Heat Mass Transfer* **33** 1183
[17] Yoon M S, Hyun J M and Park J S 2007 *Int. J. Heat Fluid Flow* **28** 262
[18] Dorfman L A and Serazetdinov A Z 1965 *Int. J. Heat Mass Transfer* **8** 317
[19] Shevchuk I V 2005 *Int. J. Therm. Sci.* **44** 374
[20] Usman M, Mehmood A and Weigand B 2020 *Int. Commun. Heat Mass Transfer* **110** 104395
[21] Lu Y W, Hu W B, Liu W L and Bai F M 2020 *Chin. Phys. B* **29** 067504
[22] Qu X R, Xu Y Y, Lü S C and Hu J M 2020 *Chin. Phys. B* **29** 046103
[23] Hayat T and Nadeem S 2016 *Chin. Phys. B* **25** 114701
[24] Li Z D, Hu Y C, He P B and Sun L L 2018 *Chin. Phys. B* **27** 77505
[25] Attia H A and Aboul-Hassan A L 2004 *Appl. Math. Model* **28** 1007
[26] Andersson H I, Korte E D and Meland R 2001 *Fluid Dyn. Res.* **28** 75
[27] Khoddamrezaee F, Motallebzadeh R and Vahid D J 2010 *J. Appl. Sci.* **10** 500
[28] Hayat T, Rashid M, Khan M I and Alsaedi A 2018 *Results Phys.* **9** 1618
[29] Li H L and Cao B Y 2019 *Acta Phys. Sin.* **68** 200201 (in Chinese)
[30] Wang Q L, Chen Y Y, Aiyiti A, Zheng M R, Li N B and Xu X F 2020 *Chin. Phys. B* **29** 084402
[31] Xi Q, Zhong J X, He J X, Xu X F, Nakayama T, Wang Y Y, Liu J, Zhou J and Li B W 2020 *Chin. Phys. Lett.* **37** 104401
[32] Wang Y, Yu X X, Wan X, Yang N and Deng C C 2021 *Chin. Phys. Lett.* **38** 094401
[33] Yang J C, Li F C, Cai W H, Zhang H N and Yu B 2015 *Chin. Phys. B* **24** 084401
[34] Zhen W K, Lin Z Z and Huang C L 2017 *Chin. Phys. B* **26** 114401
[35] Zhao J F, Luo Z Y, Ni M J and Cen K F 2009 *Chin. Phys. Lett.* **26** 066202
[36] Chen H, Li X T, Chen J Y and Shen M 2016 *Chin. Phys. Lett.* **33** 104401
[37] Rehman A and Nadeem S 2012 *Chin. Phys. Lett.* **29** 124701
[38] Mehmood A and Iqbal M S 2016 *J. Mol. Liq.* **224** 1326
[39] Alqarni A A, Alveroğlu B, Griffiths P T and Garrett S J 2019 *J. Non-Newtonian Fluid Mech.* **273** 104174
[40] Ming C Y, Zheng L C and Zhang X X 2011 *Int. Commun. Heat Mass Transfer* **38** 280
[41] Usman, Abuzar G, Irfan M, Taseer M and Yasir A 2021 *Case Stud. Therm. Eng.* **28** 101370
[42] Usman, Lin P and Ghaffari A 2021 *J. Therm. Anal. Calorim.* **146** 1735
[43] Lin Y H, Zheng L C and Chen G 2015 *Powder Technol.* **274** 324
[44] Brinkman H C 1952 *J. Chem. Phys.* **20** 571
[45] Ghasemi B and Aminossadati S M 2009 *Numer. Heat Transfer A-Appl.* **55** 807
[46] Hamilton R L and Crosser O K 1962 *Ind. Eng. Chem. Fundam* **1** 187
[47] Sheikholeslami M and Shehzad S A 2018 *Int. J. Heat Mass Transfer* **118** 182
[48] Lin Y H, Zheng L C and Zhang X X 2014 *Int. J. Heat Mass Transfer* **77** 708